HAL
open science

How do gold nanoparticles boost the performance of perovskite solar cells?

Daming Zheng, Catherine Schwob, Yoann Prado, Zakarya Ouzit, Laurent Coolen, Thierry Pauporté

To cite this version:

Daming Zheng, Catherine Schwob, Yoann Prado, Zakarya Ouzit, Laurent Coolen, et al.. How do gold nanoparticles boost the performance of perovskite solar cells?. Nano Energy, 2022, 94, pp.106934. 10.1016/j.nanoen.2022.106934 . hal-03542945

HAL Id: hal-03542945

https://hal.science/hal-03542945

Submitted on 25 Jan 2022

HAL is a multi-disciplinary open access archive for the deposit and dissemination of scientific research documents, whether they are published or not. The documents may come from teaching and research institutions in France or abroad, or from public or private research centers.

L'archive ouverte pluridisciplinaire **HAL**, est destinée au dépôt et à la diffusion de documents scientifiques de niveau recherche, publiés ou non, émanant des établissements d'enseignement et de recherche français ou étrangers, des laboratoires publics ou privés.

Cite this paper as : D. Zheng, C. Schwob, Z. Ouzitb, L. Coolen, Th. Pauporté, How Do Gold Nanoparticles Boost the Performance of Perovskite Solar Cells? Nano Energy, 94 (2022) 106934. DOI: 10.1016/j.nanoen.2022.106934

How Do Gold Nanoparticles Boost the Performance of Perovskite Solar Cells?

*Daming Zheng [a], Catherine Schwob [b], Yoann Prado[b], Zakarya Ouzit [b], Laurent Coolen [b], Thierry Pauporté [a,]**

[a] Chimie ParisTech, PSL Research University, CNRS, Institut de Recherche de Chimie Paris (IRCP), UMR8247, 11 rue P. et M. Curie, F-75005 Paris, France.

[b] Sorbonne Université, CNRS, Institut de NanoSciences de Paris, INSP, F-75005, Paris, France.

* Author for the correspondence. E-mail: thierry.pauporte@chimieparisrech.psl.eu
Website: www.pauportegroup.com

Abstract

To achieve large-scale commercialization of perovskite thin-film solar cells in the near future, improving perovskite thin-films quality and properties is becoming more and more critical. We focus here on the effect of introducing gold nanoparticles (Au_NPs) in $MAPbI_3$ layers for solar cells. Experimentally, we show a 12% improvement of the stabilized efficiency by introducing an optimized amount of Au_NPs. The nanoparticles action has been addressed through a combination of experiments and optical simulations. First, we have calculated Mie absorption coefficients, done numerical FDTD simulations and transfer-matrix simulations to model the localized surface plasmon resonance (LSPR) and light scattering efficiency of Au_NPs. They have allowed us to state that to reach a significant beneficial effect, the nanoparticle volume ratio must be above 1%, which is far above the content in our optimized perovskite solar cells layers. Only a negligible enhancement of light absorption can be attributed to the Au_NPs. Secondly, by combining several analysis techniques, especially by using glow discharge-optical emission spectroscopy (GD-OES), we reveal the mechanism of how Au_NPs improve the quality of perovskite films. The gold nanoparticles lead to the formation of monolithic grains with few defects and reduced grain boundaries which are the targeted properties for high efficiency. Therefore, in our devices, the effect of Au_NPs on the improvement of the quality of the perovskite layer is far more significant than that of the increase in light-harvesting. Finally, further performance and stability increases have been achieved by introducing the treatment of Au_NPs/$MAPbI_3$ film surface by n-propylammonium iodide (PAI). It resulted in a power conversion efficiency of over 20%.

Cite this paper as : D. Zheng, C. Schwob, Z. Ouzitb, L. Coolen, Th. Pauporté, How Do Gold Nanoparticles Boost the Performance of Perovskite Solar Cells? Nano Energy, 94 (2022) 106934. DOI: 10.1016/j.nanoen.2022.106934

Keywords : Perovskite solar cells; Gold nanoparticles; Growth mechanism; Localized surface plasmon resonance; Glow discharge-optical emission spectroscopy.

1. Introduction

During the past decade, organo-metal halide perovskites (PVKs) have risen as one of the most promising semiconductor families for photovoltaic solar cells due to their strong optical absorption, good carrier mobility, weak exciton binding energy and low processing costs.[1-11] Component and additive engineering has been extensively developed and have greatly helped perovskite solar cells (PSCs) to make a huge step forward high efficiency and commercialization. Until now, the highest certified power conversion efficiency (PCE) achieved is 25.5%.[12] However, PSCs still need further progress to overcome instability caused by moisture, oxygen and heat, without reducing the efficiency. This requires notably the need for improved crystalline quality of the perovskite layer.

The use of plasmonic nanomaterials is frequently proposed as a means to improve the absorption of the active layer and then enhance the performance of photovoltaic devices. [13−18] In particular, the use of plasmonic materials and arrangements of them have been explored for almost all types of solar cells,[19] either for solid-state[20,21] or solution-containing ones.[22−25] In photovoltaic devices, an efficient light management can be accomplished by 1) reduction of reflection losses at the cell surface and 2) trapping light in the absorbing layer.[26,27] The localized surface plasmon resonance (LSPR) of plasmonic nanoparticles can enhance light absorption, either by electromagnetic field enhancement near the particle or by light scattering into trapped optical modes [28,29], and could theoretically improve the photovoltaic performances of solar cells. Many groups have reported the successful application of plasmonic materials to perovskite solar cells (as reviewed in refs[30-36]) and have reported photovoltaic efficiency relative improvements ranging from 0.6 % to 40 %. However, the understanding of the underlying mechanisms responsible for these improvements remains incomplete. While addition of plasmonic particles has been motivated by the desire to enhance light absorption, it is still unclear whether the main effects are optical or electrical.[36] Many optical discussions are limited to qualitative LSPR simulations and only a few papers compare simulations and experimental results both qualitatively and quantitatively.[37,38] Apart from light absorption, the influences of the particles on exciton dissociation [38], charge transport and collection [36] have also been discussed. Few reports have paid attention to the influence of plasmonic materials on the perovskite film itself, such as the crystal growth [39] or stability [30,36]. Whether gold nanoparticles can effectively improve the crystallinity of perovskite is still under debate. Using a relatively high concentration of NPs, some researchers did not find any enhancement on crystallization [40-45], especially from x-ray diffraction (XRD) results. However, some others found that NPs affect grain size, PbI_2 formation and crystallinity of the perovskite film [46]. In the research results, so far, there is

no systematic study on how nanoparticles affect the crystalline quality of perovskite films and whether this can have an effect on the overall absorption of the film and the performance of PVK.

In this work, we comprehensively analyze the effect of Au_NPs inclusion in model $MAPbI_3$ PVK films through the combination of simulation and experiments. We have studied systematically how Au_NPs affect the solvent evaporation and the film growth direction in the process of film formation by glow discharge-optical emission spectroscopy (GD-OES). Due to its low detection limit (10 µg/g), depth profile analysis (up to a thickness of 100 µm) and large detection area (ten square millimeters), this technique allowed us to know the situation of the entire perovskite layer at every moment of their preparation process. By combining with scanning electron microscopy (SEM), XRD, differential scanning calorimetry (DSC), energy dispersive X-ray analysis (EDX) and other test results analysis, we have determined the mechanism responsible for the effect of the Au_NPs on the growth of the $MAPbI_3$ layer. On the other hand, various optical models have shown us that, in our systems, only a negligible portion of the photovoltaic improvement can be assigned to the plasmonic enhancement of absorption. Therefore, we have concluded that the impact of Au_NPs on light absorption through the improvement of the quality of the perovskite layer is far more significant than that of the plasmonic increase in light-harvesting.

Finally, to further enhance the performance of the PSCs, we employed a post-treatment technique, leading to the formation of a quasi2D capping layer on the top surface of the $MAPbI_3$ perovskite layer. We introduce the surface treatment of $MAPbI_3$ by n-propylamine hydroiodide (also called n-propylammonium iodide, noted PAI). The 2D $(PA)_2MA_2Pb_3I_{10}$ capping layer forms a barrier that protects from degradation the underneath 3D perovskite films and mitigates exciton recombination. We show that it boosts the Au_NPs/$MAPbI_3$ composite solar cell efficiency and stability (this study is detailed in the **Annex A**, Supporting Information).

2. Results and Discussion

2.1 Perovskite solar cells

$MAPbI_3$ was chosen as a well-documented perovskite photovoltaic compound and used as a reference. A first difficulty was to introduce the nanoparticles homogeneously in the layer and at a sufficient concentration. Water, the solvent employed for the synthesis of the nanoparticles is detrimental for the perovskite film quality. Therefore, we proceeded in the water solvent exchange by DMSO, the solvent employed in the perovskite precursor. By a centrifugation/evaporation process, we prepared a suspension of Au_NPs in DMSO, with a concentration of ~7.10^{-7} M. The concentration factor was 252 compared to the initial aqueous suspension. This solution was dark red as expected for non-aggregated and stabilized NPs. We noted that for higher concentrations, during the evaporation of water and replacement by DMSO, the solution turned purple, indicating aggregation of the NPs. TEM

was employed to reveal the morphology and size of the gold nanoparticles (**Figure 1a**). They presented a spherical shape and their size distribution is given in **Figure 1b**. Most gold nanoparticles were 13~16 nm in diameter (average at 14.3 nm) and it resulted in a [Au]~0.06 M. A certain volume of Au_NPs, namely 15 µL, 30µL or 45 µL, was added to the perovskite precursor solution, perfectly mixed and the resulting perovskite precursor solution (PPS) was employed to prepare the composite films. The homogeneous integration of Au_NPs throughout the layer thickness was proved by GD-OES measurements as shown later. We noted that, at higher concentration, the film morphology and properties were degraded and could not suit efficient solar cells.

The best photovoltaic performances of the reference PSC and of the various Au_NPs/$MAPbI_3$ PSCs are gathered in **Table 1.** Those of the reference cell (Ref) were moderate, with a *PCE* measured at 17.25 % on the reverse scan. After the introduction of Au_NPs, all the parameters of the solar cell were enhanced, especially the open-circuit voltage (V_{oc}) and the short circuit current (J_{sc}). At the highest investigated NP loading the performances dropped with a PCE at 13.9 %. An optimum for V_{oc}, J_{sc} and fill factor (*FF*) was obtained for Au_NPs-30. It resulted in a best *PCE* measured on the reverse scan above 19% (**Table 1** and **Figure 1c**). These results were confirmed by the statistical analysis provide in **Figure 1 e-i**. The effect of Au_NPs on the *Jsc* was confirmed by the external quantum efficiency (*EQE*) spectra and their integration (**Figure S1**, Supporting Information). The NPs had no significant effect on the hysteresis amplitude of the *J-V* curves quantified by the hysteresis index (*HI*) (**Table 1** and **Figure 1h**).

Table 1. *J-V* curve parameters, PCE and hysteresis index of champion solar cells.

Name	Capping layer	Scan direction	V_{oc} [V]	J_{sc} [mA. cm^{-2}]	*FF*	PCE [%]	*HI(%)* [a)]
Ref	No	Reverse	1.037	21.83	76.32	17.25	17
		Forward	1.001	21.81	65.24	14.24	
Au_NPs-15	No	Forward	1.042	22.47	75.62	17.70	16
		Reverse	1.032	22.23	64.73	14.84	
Au_NPs-30	No	Forward	1.059	23.37	78.1	19.01	16
		Reverse	1.047	23.11	66.12	16.02	
Au_NPs-45	No	Forward	1.035	19.58	68.64	13.91	13

		Reverse	1.011	19.69	60.62	12.07	
Au_NPs-30/PAI	Yes	Forward	1.103	23.26	79.68	20.44	13
		Reverse	1.091	23.14	70.42	17.78	

[a)] Hysteresis Index, noted HI, defined as $(PCE_{Rev}-PCE_{For})*100/PCE_{Rev}$

To further improve the performances of the best system, we introduced the surface treatment of the composite layer by a solution of n-propylammonium iodide (PAI) in isopropyl alcohol (IPA). To our knowledge, PAI treatment has only been applied yet to surface treatment of $Cs_{0.1}FA_{0.9}PbI_3$ [47] and $Rb_{0.05}Cs_{0.1}FA_{0.85}PbI_3$ perovskite films [48]. The full optimization and characterization study for the Au_NPs-30 cell is detailed in the **Annex A** (Supporting Information). We found that 4 $mg.mL^{-1}$ was the best concentration for which it resulted in a best PCE of 20.44% (**Table 1** and **Figure 1i**). The statistical analysis in **Figures 1e-i** reveals that this treatment mainly improves the cell V_{oc} and the *FF*, while the J_{sc} is unchanged. The optimized treated films and devices are noted Au_NPs-30/PAI, hereafter. We characterized the surface layer as composed of quasi-2D $(PA)_2MA_2Pb_3I_{10}$ perovskite in the **Annex A** (Supporting Information). The surface became smoother after the post-treatment not only because of the height difference caused by the reduced stacking of the grains, but, more essentially, because the small organic molecule used in the post-treatment recrystallize the grain boundary and suppress defects (**Figure S3**, Supporting Information). It results in less recombinations and then higher V_{oc} and *FF* parameters.

Cite this paper as : D. Zheng, C. Schwob, Z. Ouzitb, L. Coolen, Th. Pauporté, How Do Gold Nanoparticles Boost the Performance of Perovskite Solar Cells? Nano Energy, 94 (2022) 106934. DOI: 10.1016/j.nanoen.2022.106934

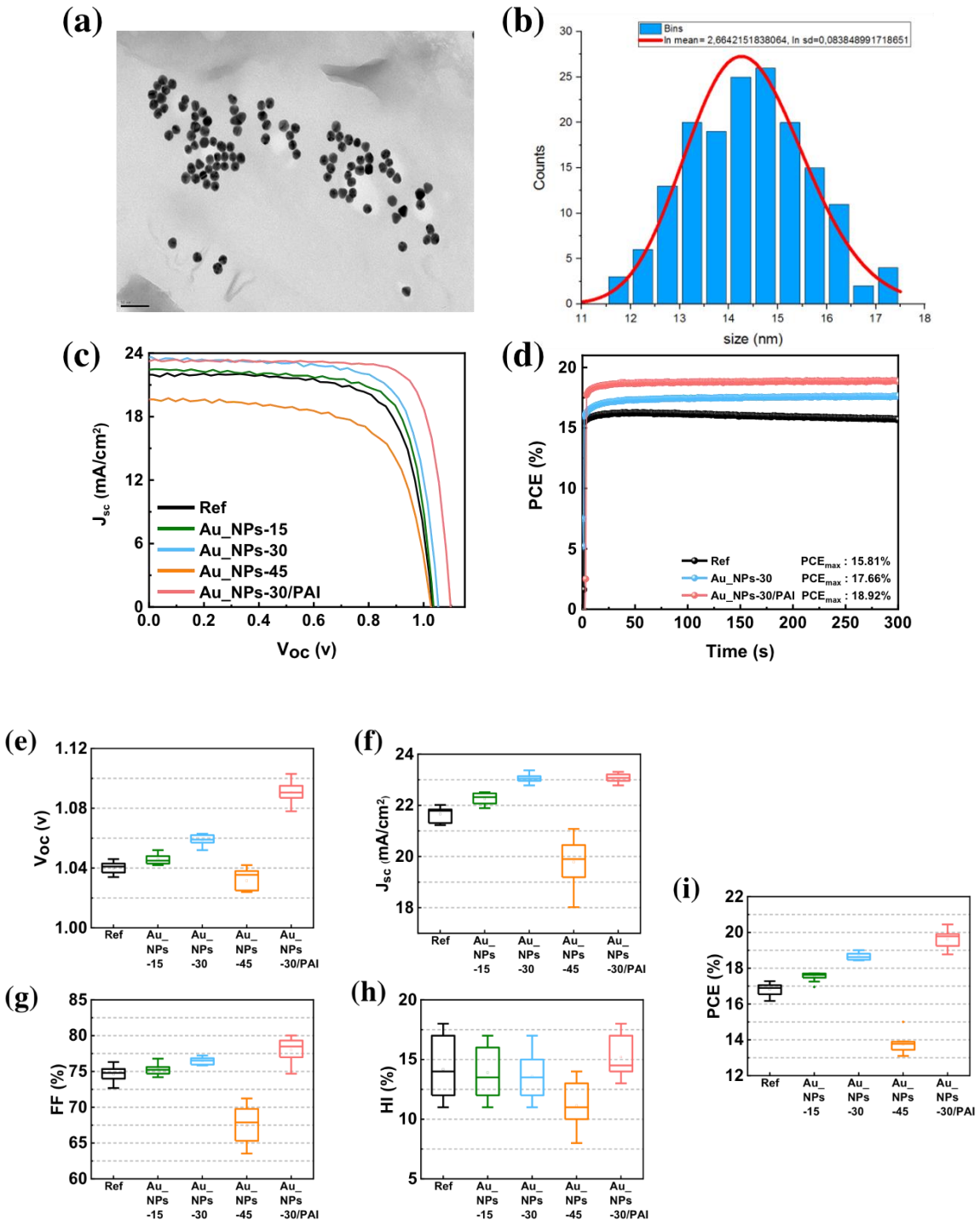

Figure 1. (a) TEM view images of gold nanoparticles. (b) Statistical grain size analysis. (c) *J-V* reverse curves. (d) Maximum power point (MPP) tracking and best-stabilized efficiency. (e-i) Statistical analysis of the optimized PSCs *J-V* curve parameters and PCE.

The *PCE* tracking at the maximum power point and corresponding steady-state *PCE* are disclosed in **Figure 1d**. We first noticed that the Au_NPs-30/PAI sample with PAI post-treatment exhibited the

best *PCE* (18.92%) compared to Au_NPs-30 (17.66%). The Ref cell had a moderate *PCE* of only 15.81%. We also see that the overall trend of Ref cell steady-state *PCE* decreased with time, revealing a rather poor stability (**Figure S1b**, Supporting Information). On the other hand, we found that the efficiency of the Au_NPs-30 and Au_NPs-30/PAI devices increased slightly with time. It suggests some initial interfacial reorganization before stabilization and improvement (the detailed analysis is presented in **Annex A**, Supporting Information).

Also, importantly, we investigated the stability of the various perovskite films. The highly demanding stability test in high humidity environment (RH ≥ 90%) was implemented on Ref, Au_NPs-30 and Au_NPs-30/PAI in **Figure S5d-f** (Supporting Information). We found that the use of Au_NP significantly improved the stability by delaying the appearance of the PbI_2 phase. The stability was further improved when the perovskite film underwent a surface treatment with PAI: the PbI_2 peak at 12.7° was strongly reduced then compared to the other samples.

We will now focus on the beneficial effect of Au_NPs and consider in detail different potential origins of the performance enhancement, starting with the optical absorption.

2.2. Effects of Au_NP on $MAPbI_3$ film optical properties

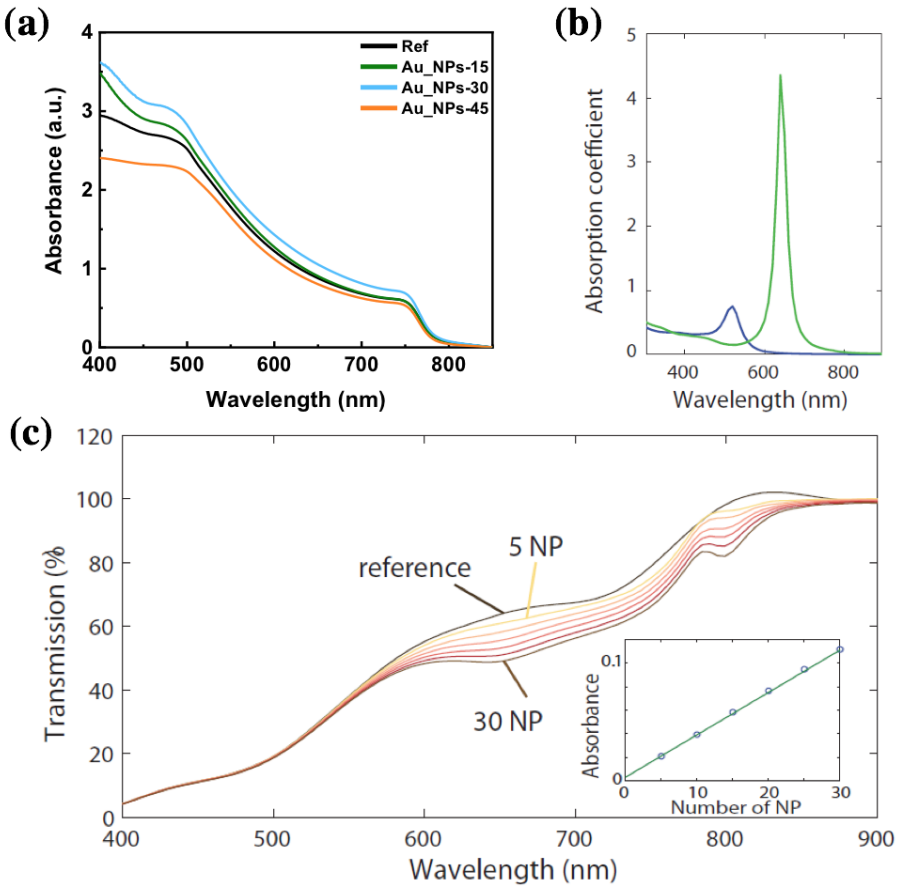

Figure 2. (a) Absorbance of reference, Au_NPs-15, Au_NPs-30 and Au_NPs-45 layers. (b) Absorption coefficient spectrum obtained from Mie's theory for a gold nanosphere of radius 7 nm in water (blue curve) or in a dielectric medium of index equal to the real component of the $MAPbI_3$ optical index (green curve). (c) Transmission through a 100-nm layer of $MAPbI_3$ (200x200 nm² area) containing 5, 10, 15, 20, 25 and 30 of 7-nm radius gold nanoparticles (yellow to brown curves) and without nanoparticles (black, reference). Inset: additional absorbance ($-\log_{10} T/T_{Ref}$, averaged over 650-670 nm) as a function of the number of nanoparticles.

The effect of the Au_NP on light absorption by the cell is evidenced in the *EQE* spectra (**Figure S1**, Supporting Information). A strong photovoltaic effect is observed over the visible spectrum, with a drop around 800 nm corresponding to the band gap of $MAPbI_3$. Around 500 nm, the *EQE* reaches a maximum close to 89 %. It drops at lower wavelengths due to light absorption by the transparent conducting electrode [49]. In the 600-800 nm range, the *EQE* decreases down to 70 % for the Ref cell because of the lower $MAPbI_3$ absorption coefficient [49]. The *EQE* in this range is increased for the Au_NP-15 and -30 cells: the fact that the increase occurs in the range where the $MAPbI_3$ absorption coefficient is lower than typical of an enhanced optical absorption. On the other hand, for the Au_NP-45 cell, the *EQE* is decreased over the entire visible spectral range: this suggests a decrease of the cell's electrical performance rather than of the optical absorption.

A simple mechanism by which the inclusion of Au_NPs may increase the *PCE* would be if they influence the thickness of the $MAPbI_3$ layers. Indeed, the cross-sectional SEM profiles show a 320-nm thickness for $MAPbI_3$ reference sample (**Figure 6a**) and a 355-nm thickness for the Au_NPs-30 sample (**Figure 6b**). The performance enhancement could be explained by whole absorbance spectrum enhancement related to a thickness increase. To address this issue, we modelled the effect of thickness on the transmission spectrum, and then on J_{sc}, in the **Annex B** (Supporting Information). We found that an increase of 40 nm in $MAPbI_3$ thickness would lead to around a 0.2 mA/cm² increase of J_{sc}, while our experimental EQE results give a 1.4 mA/cm² increment (**Figure S1,** Supporting Information). Therefore, this effect can only contribute partially to the observed *PCE* improvement, and one must also consider the intrinsic absorption properties of the perovskite material.

In the literature on PSCs containing metal NPs, many reports have attributed the increased *PCE* to enhanced light absorption by the perovskite layer due to localized surface plasmon resonance (LSPR) and light scattering.[26-28,30-37] **Figure 2a** shows the measured absorbance spectra of the Ref and Au_NPs layers. These spectra share features similar to typical perovskite films with an absorption edge at around 785 nm. The introduction of Au_NPs increased the film absorbance with a best result for 30 µL. When the addition of gold nanoparticles increased to 45 µL, the absorption of perovskite film decreased markedly. The comparison of the Ref and Au_NPs-30 samples shows that the enhancement occurs throughout the whole absorption UV/Vis spectrum. No absorption peak, as would be expected for a LSPR effect, is found. To clarify this point, we calculated theoretically the absorption of 14 nm diameter-sized gold nanoparticles. Different theoretical approaches can be used to model the influence of the Au_NPs on the solar cells' optical properties. First, we plot in **Figure 2b** the absorption coefficient spectrum obtained from Mie's analytical equations. The NP absorption is strongly dependent on the surrounding medium. In water, the LSPR resonance is centered at 520 nm, while it shifts to 640 nm if the surrounding dielectric medium has the real optical index component of $MAPbI_3$.[49]

In order to take into account $MAPbI_3$'s imaginary optical index component, we performed finite-difference time-domain (FDTD) simulations of a $MAPbI_3$ layer of thickness 100 nm and area 200x200 nm² (**Figure 2c**). For the bare $MAPbI_3$ layer, the transmission is low in the blue range because of the strong $MAPbI_3$ absorption. It increases up to 100 % for wavelengths above the bandgap (with some values slightly larger than 100 % due to numerical artifacts). When 7-nm radius gold nanoparticles are introduced in the layer, the transmission is decreased in the 550-800 nm range. It decreases more and more as more particles are present, with around a 20 % additional absorption for 30 NPs, which corresponds to a 1 % gold volume fraction in $MAPbI_3$. This decrease occurs with a dip at 650 nm, agreeing with Mie's theory, and can be attributed to the LSPR resonance. As compared to Mie theory, the LSPR effect occurs on a much broader spectral range according to FDTD calculations, possibly because taking into account $MAPbI_3$'s imaginary optical index lowers the resonance quality factor.

It is noteworthy that this additional absorption may be due either to enhanced $MAPbI_3$ absorption or to plasmon dissipation in gold, the former leading to enhanced *PCE*. At the same time, the latter should correspond to losses (unless the plasmon's energy is converted into hot carriers). The light absorption within a given volume can be calculated from FDTD simulations as:

$$Abs = \iiint_V \|\vec{E}\|\varepsilon'' dV$$

(ε'' being the imaginary component of the local relative permittivity). **Table 2** shows the additional absorption in a 100x100x100 nm^3 volume of $MAPbI_3$ when adding a Au_NP. At 500 nm wavelength so at off-LSP-resonance, both absorption changes are meager. At 640 nm, so at the LSP resonance, 40 % of the additional absorption occurs in the Au_NPs, while 60 % of the extra absorption corresponds to useful $MAPbI_3$ absorption.

Table 2. Calculated additional absorption in a 100x100x100 nm^3 $MAPbI_3$ volume when adding a Au NP, under different wavelengths and either within the volume of gold or $MAPbI_3$.

Wavelength (nm)	**Additional absorption in the Au_NPs [%]**	**Additional absorption in the $MAPbI_3$ [%]**	**Total Additional absorption [%]**
500 (Off-resonance)	+0.2%	-0.1%	+0.1%
640 (LSP resonance)	+1.5%	+2.2%	+3.7%

The inset of **Figure 2c** plots the additional absorbance as a function of the number of nanoparticles. Fitting the inset of **Figure 2c** with Beer's law (Absorbance = $lc(N_A/\ln 10)\sigma_{abs}$) yields an absorption cross-section of 340 nm². The LSPR absorption cross-section from Mie's theory (absorption coefficient $\times\ \pi R^2$ = 677 nm²) is of the same order of magnitude, but somehow larger, possibly because of its higher quality factor. In our experiment, the calculated volume fraction of gold nanospheres in $MAPbI_3$ in the optimal 30 µL case (sample Au_NPs-30) is only 0.009 % (**Annex C**, Supporting Information), so 100 times lower than simulated in **Figure 2c** with 30 NPs. Therefore, the absorption modification induced by the LSPR can be considered as negligible in our experimental solar cell. In other words, the $MAPbI_3$ layer contains one NP per $5x10^4$ nm² surface, which is much larger than the LSPR absorption cross section, so that the NP influence on absorption is negligible.

As a conclusion for this section, the *EQE* spectra suggest that the improved *PCE* for the Au_NP-30 cells is due to enhanced light absorption, while the *PCE* decrease of the Au_NP-45 can be attributed to electric losses. By using various optical models, we have shown that this absorption enhancement cannot be attributed to LSPR effects because the NP concentration is weak and that the $MAPbI_3$

thickness increase is rather insufficient. We propose in the following sections that the increased light absorption is due to an improved $MAPbI_3$ growth and crystalline quality.

2.3. Morphology, crystallinity, defects and charge recombination in the PSC

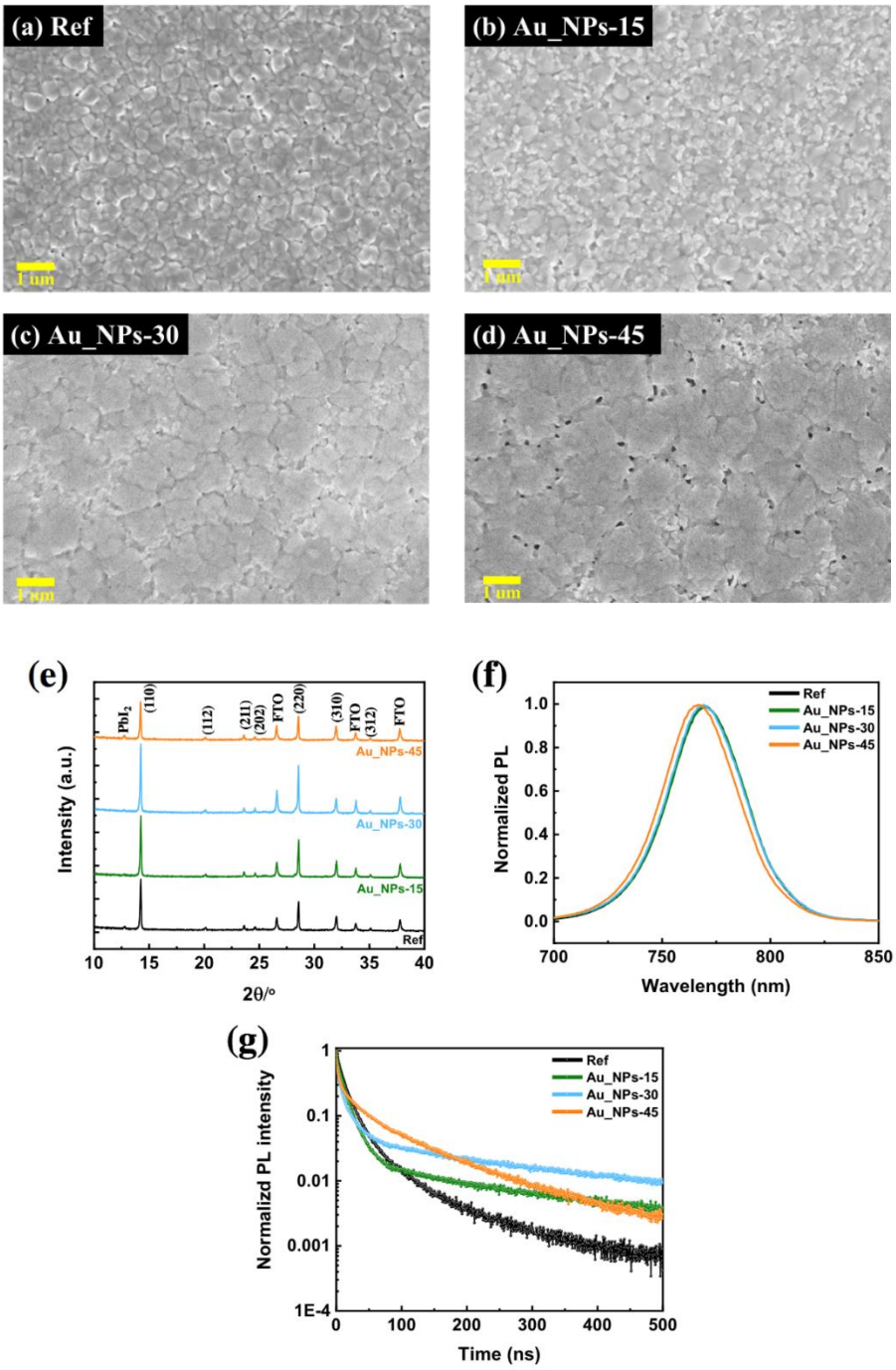

Figure 3. (a-d) SEM top-view images of perovskite layers prepared with different volume of Au_NPs: (a) Ref, (b) Au_NPs-15, (c) Au_NPs-30, (d) Au_NPs-45 (the scale bar is 1 µm). (e) XRD patterns for different volumes of Au_NPs added to the perovskite precursor solution. (f) Steady-state PL. (g) TRPL curves of Ref, Au_NPs-15, Au_NPs-30 and Au_NPs-45 samples (the samples are deposited on Glass).

Figures 3a-d shows the effect of different volumes of Au_NPs on the film morphology. The Ref sample presented small-size perovskite grains with pinholes between them. These pinholes did not cross the full perovskite layer and were due to the irregular stacking of the crystals caused by the excessive growth of PbI_2 during the film formation process. The perovskite was non-compact and its surface was rough. After introducing 15 µL Au_NPs in the perovskite precursor solution, a lot of small grains were distributed among the large island-like grains (**Figure 3b**). It seems that the Au_NPs inhibited the fast crystallization of perovskite film. When 30 µL Au_NPs was added (**Figure 3c**), these tiny grains in **Figure 3b** were reduced significantly and replaced by large compact island-like crystals of ~2 µm in size. Increasing the volume up to 45 µL led to a further increase of the grain size, but many voids appeared between them (**Figure 3d**). The above analysis was confirmed by AFM measurements (**Figure S3**, Supporting Information). The measured RMS roughness of the Ref sample was 30.6 nm while it decreased to 24.3 nm for the optimized sample with embedded Au_NPs. These values are consistent with top-surface SEM images.

The structural properties of the layers were investigated by XRD and the measured patterns are displayed in **Figure 3e.** With the increased volume of Au_NPs, the (110) peak of $MAPbI_3$ gradually increased, while the intensity of the PbI_2 peak at 12.6 ° gradually decreased. The increase in strength signs a higher quality of the perovskite film and it proves that 30 µL of Au_NPs can suppress PbI_2 growth and maximize the crystallinity. We also found that too much Au_NPs is detrimental to the layer quality. It is manifested by the appearance of the PbI_2 peak in the Au_NPs-45 sample pattern and the decrease of the intensity of the (110) peak. These results are consistent with the morphology obtained by SEM (**Figure 3**). EDX analyses were also implemented to determine the composition of perovskite layers (**Table S2**, Supporting Information). Since the $MAPbI_3$ components are relatively simple, we only focused on the I/Pb atomic ratio for Ref and Au_NPs-30 samples. In theory, the closer this value is to 3, the higher is the crystal quality and purity. In order to make the test data more accurate, we selected five different positions on the perovskite surface of 100µm * 100µm measurement size and then took the average value. We found 2.79 ± 0.10 for the Ref sample and 3.01± 0.05 for the Au_NPs-30 sample. The latter had a value close to the stoichiometry and was a high-quality perovskite layer. The lower value for the Ref sample is assigned to the presence of PbI_2 in agreement with the XRD result. The peak of PbI_2 appeared in the XRD patterns of Ref (**Figure 3e**).

Figure 3f shows the PL spectra measured at an excitation wavelength of 500 nm from the perovskite side and at room temperature. There is a slight blue shift in the emission peak of the Au_NPs samples compared to the Ref sample which is in good agreement with the enlargement of the measured optical

band gaps (**Figure S7b**, Supporting Information**)**. Furthermore, the PL decay profiles of $MAPbI_3$ films without and with the presence of Au_NPs are displayed in **Figure 3g**. The PL decay data were adequately fitted using a triple-exponential function and the results are shown in **Table S3 (**Supporting Information**)**. τ_{slow} is related to the bulk recombination and then defect density. We observed two important phenomena: τ_{slow} was 62 ns for Ref, while it was much longer at 323 ns for the Au_NPs-30 sample. This increase indicates a much better bulk structural quality of the perovskite when Au_NPs were present. Moreover, the relative contribution of τ_{slow} (RC_{slow}) was increase from 26% to 92 % with the Au_NPs. Therefore, the other recombinations pathways were strongly suppress in the optimized composite. We also noted that a too high amount of Au_NPs decreased these two parameters to 90 ns and 85 %, respectively for the Au_NP-45 sample.

Figure S8 presents the electrical impedance spectra of the two PSCs measured under light illumination and at 0.5V and 0.8V applied voltages. In both cases the impedance was higher for the Au_NPs-30 device than for the Ref device. For instance, the high frequency resistance increased from 178 Ω to 1105 Ω at 0.5V and from 74 Ω to 405 Ω at 0.8V. We have shown elsewhere [8] that the electrical impedance of a PSC is mainly related to recombination phenomena occurring in the devices. The increase of the Au_NPs-30 cell impedance expresses a decrease of the charge recombinations.

From the above results, we can conclude that the Au_NPs significantly influence the properties of the perovskite layer. The addition of an appropriate volume of Au_NPs increases the grain size and there are statistically less grain boundaries which are rich in defects that act as recombination centers. It also improves the perovskite bulk quality and reduces native defects. It results in a higher cell V_{oc}. The structural improvement of the perovskite film is beneficial for photo-induced charge carrier transportation and separation. We now focus on the origin of these improvements.

2.4 Main inorganic elements distribution upon thermal annealing

The above study shows the strong effect of Au_NPs on the $MAPbI_3$ film formation, on the final morphology, grain density and size as well as on the structure and defect density. All these aspects strongly influence the final performances of the devices. To get a deep understanding of the effect of Au_NPs on the film formation process, we employed the GD-OES technique. We first followed the movement of main elements composing the perovskite layer upon the thermal annealing process. Through the distribution of these elements and the motion behavior, we have been able to understand better the process of crystallization and the quality of the perovskite layer. At the same time, we have also been able to probe the gold nanoparticles distribution in the layer. Secondly, in the next section, by tracing the sulfur element of DMSO, we will determine the growth direction of the $MAPbI_3$ film and explain the effect of Au_NPs on the growth process.

Figure 4 presents the movement of primary elemental ions for the Ref and the Au_NPs-30 samples upon thermal annealing. The presence of Ti is superimposed as a dotted line. It visualizes the start of the mesoporous layer at around 25-30 s sputtering time. Therefore, sputtering times between 0 and 20-25 s correspond to downward probing of the perovskite layer. We first followed Au and found that the gold nanoparticles were distributed over the whole precursor layer before thermal annealing. The prominent peak gradually changes to give two broad peaks, one localized on the mesoporous TiO_2 and a bigger one above. Therefore, according to GD-OES, the gold nanoparticles were not well-diffused near the interface between the pure perovskite and the perovskite/titanium oxide layer. Some mesoporous titanium dioxide layer enrichment occurred at the beginning of the thermal annealing (**Figure 4a**). **Figures 4b** and **4c** show the distribution of Pb. For the Ref sample, Pb distribution spreads with time and, also, splits into two peaks. It can be explained based on DSC measurements (**Figure 5**). The low temperature of the first peak shows the fast solvent removal and it is combined with a slow crystallization (second peak) (**Figure 5a**). These lead to a stack of multiple crystals in the depth direction of the perovskite layer. After addition of Au_NPs, the GD-OES peak also spreads during the first 10s and then Pb remain homogeneously distributed throughout the layer (**Figure 4c**). DSC measurements (**Figure 5b**) reveal that the solvent is then more slowly removed from the layer (first peak) and that the crystallization (second peak) is sped up, which makes the perovskite film homogeneous.

We can also see that the iodine (I) signal is increased during the first seconds due to the strong solvent elimination and the broad distribution of I in both samples (**Figure 4d** and **Figure 4e**). By comparing **Figure 4f** and **4g**, we can conclude that the high quality of the Au_NPs-30 perovskite layer produces an enhanced signal intensity with a broader distribution for each element.

Cite this paper as : D. Zheng, C. Schwob, Z. Ouzitb, L. Coolen, Th. Pauporté, How Do Gold Nanoparticles Boost the Performance of Perovskite Solar Cells? Nano Energy, 94 (2022) 106934. DOI: 10.1016/j.nanoen.2022.106934

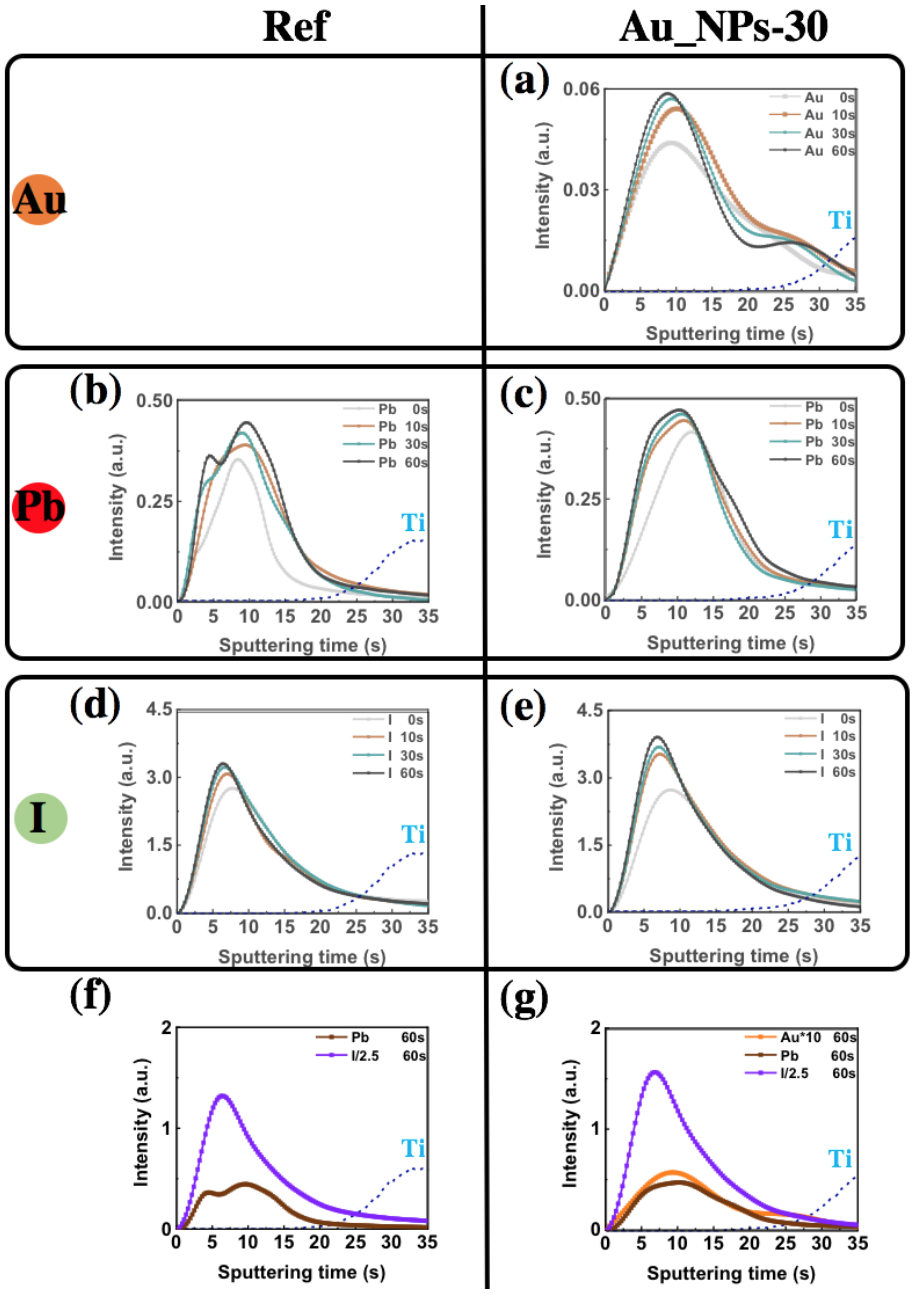

Figure 4. GD-OES distribution curves of the main elements composing the perovskite film at various thermal annealing times: (a) Gold, (b, c) Lead and (d, e) Iodine. (f, g) After the 60s of annealing, (f) Ref and (g) Au_NPs-30. In (f) and (g) the intensity of Au is multiplied by ten and the intensity of I divided by 2.5 for clarity. The thermal annealing time is given in seconds. (Dashed line in (a-g): Ti profile corresponding to the *meso*-TiO_2).

2.5 Solvent elimination and film formation upon thermal annealing

Differential Scanning Calorimetry (DSC) provided us further information on the effect of Au_NPs on the formation of well-crystallized perovskite films. The curves were measured on the two samples prepared as powders' adducts (**Figures 5a-b**). A first endothermic peak was observed at ~79.8°C for the Ref sample, and assigned to the evaporation of DMSO (DMF was eliminated upon washing the

adducts by diethyl ether)[26] since DMSO mixed with PbI_2 has been shown to start to evaporate at a temperature as low as 75°C.[38] This peak was also found for the Au_NPs-30 sample but at higher temperature (83.3°C). It suggests that the presence of Au_NPs prolongs the period of solvent evaporation. The evaporation temperature increased by 3.5°C with Au_NPs introduced into the PPS. This means that the presence of gold nanoparticles renders more difficult the evaporation of the surrounding DMSO solvent. To prove this, we performed a DSC test on a solution of Au_NPs in DMSO. In **Figure S9** (Supporting Information), the endothermic peak of Au_NPs was measured as high as 172.8°C, which is much higher than 79.8°C.

Next, we observed on **Figure 5a** a second endothermic peak, measured at 99.7°C for the Ref sample, which corresponds to a long phase change process from ~81°C to ~104°C. This endothermic peak is assigned to the perovskite crystallization. Interestingly, the sample with Au_NPs presented a sharp endothermic peak at 92.7°C, therefore at a 7°C lower temperature than the Ref one. Moreover, this sample had a short phase transition period. The shortening of the phase transition process indicated a faster crystallization rate. Because of this gap, the quality of our thin films changed considerably. In the case of the Ref $MAPbI_3$ system, the conventional crystallization rate led to excessive growth of lead iodide, resulting in the stacking of grains. On the contrary, the situation can be avoided by slowing the solvent elimination and accelerating the crystallization rate properly by introducing Au_NPs.

The residual solvent elimination is an essential aspect of film formation control upon thermal annealing and is at the origin of the film crystallization and growth. The fate of DMSO was tracked by following the S element which, in the investigated system, is only present in DMSO. The GD-OES S element profile is presented in **Figures 5c-f** for the various films and various annealing times. Before thermal annealing, the DMSO profile was asymmetrical in every case, and we observed that the outer part of the film was more affluent in solvent than the inner part. For the thermal annealing, our results distinguished two stages. The Stage-1 occurred during the first 10 s of annealing on a hotplate upon which the initial film changed from translucent light yellow to brown (**Figure S10**, Supporting Information). During this stage, the most superficial residual solvent evaporates and is strongly eliminated at the uttermost surface. Moreover, the XRD patterns in **Figure S11** (Supporting Information) show an amorphous precursor with only a very small diffraction peak at 11.8° which can be assigned to an intermediate phase mixing Pb-I-DMSO.[50] This peak disappears upon the first 10 s of thermal annealing while the peak at 14.1°, assigned to the (110) $MAPbI_3$ reflection, arises and grows because the $MAPbI_3$ phase nucleates and growths in all the directions during this period.

The next stage (Stage-2) corresponded to 10 s to 60 s annealing time, when the film became black. We observed a conspicuous effect of Au_NPs on the solvent distribution upon annealing. In the case of the Ref sample, DMSO is eliminated fast near the surface (**Figure 5e**), the film grows downward (top to down). For the Au_NPs-30 sample, after 10s, the profile evolution shows a homogeneous elimination of DMSO throughout the layer (**Figure 5f**). We can conclude that the film growth is then

Cite this paper as : D. Zheng, C. Schwob, Z. Ouzitb, L. Coolen, Th. Pauporté, How Do Gold Nanoparticles Boost the Performance of Perovskite Solar Cells? Nano Energy, 94 (2022) 106934. DOI: 10.1016/j.nanoen.2022.106934

lateral. In all cases, most of the solvent was eliminated after 4 min (**Figure S12**, Supporting Information).

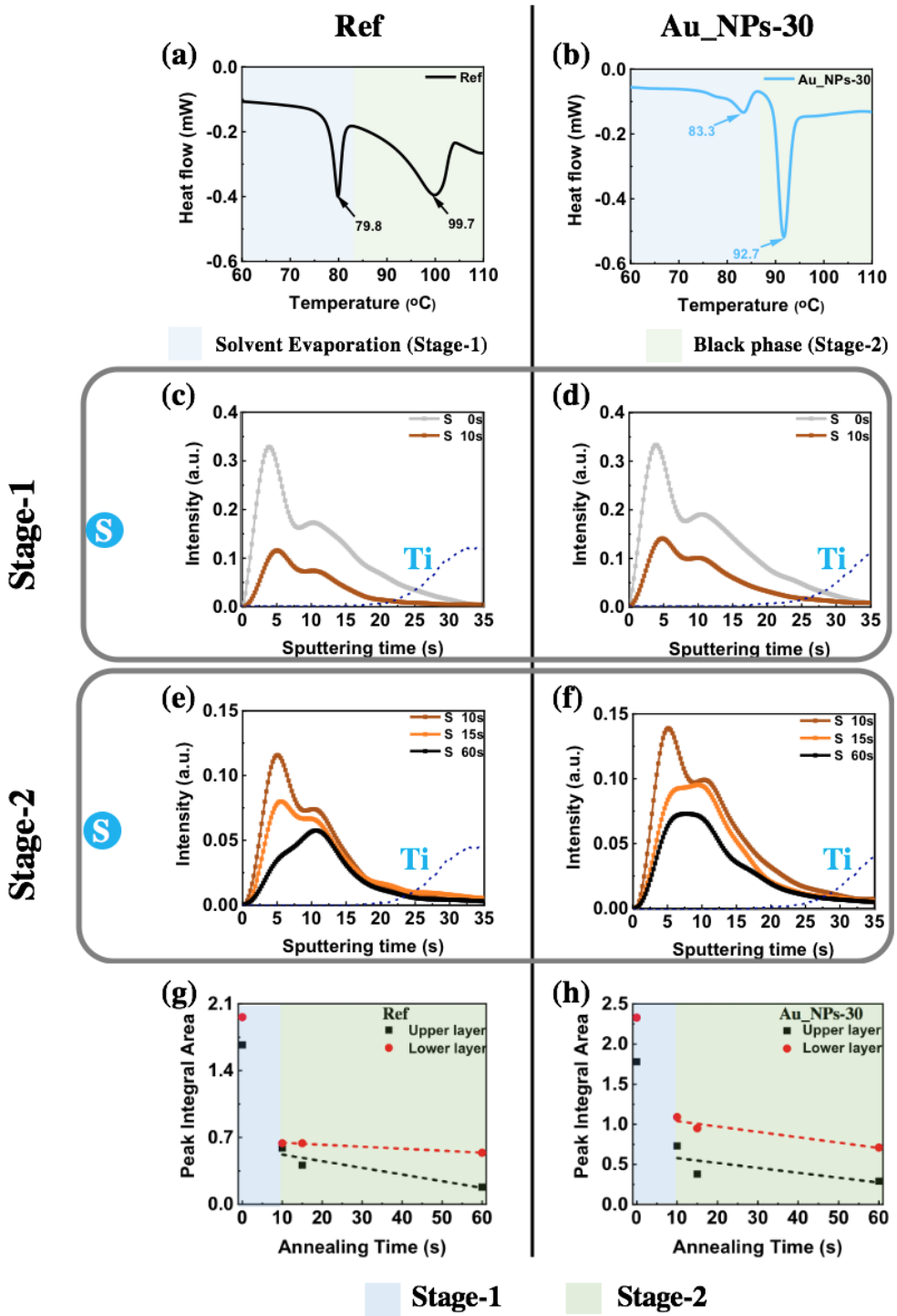

Figure 5. DSC curves of (a) Ref, (b)Au_NPs-30 sample adducts. (c-f) Evolution of GD-OES S profile in the (c,e) Ref and (d,f) Au_NPs-30 perovskite precursor layer upon thermal annealing. The dashed line in (c-f) is the Ti profile corresponding to the *meso*-TiO_2. (g,h) Peak integral area of the upper layer and lower layer at different annealing times. (Black dashed lines are the linear fit lines of the upper layer in Stage-2; Red dashed line are the linear fit lines of the lower layer in Stage-2.)

In the profiles displayed in **Figures 5c-f**, we observed an apparent strong effect of the Au_NPs on the solvent distribution upon thermal annealing. To refine the analysis, we developed quantitative tools for a sound S (Sulphur) change investigation. We divided the layer into an upper part and a lower part, as described in **Figure S13** (Supporting Information) and the related comment. We report in **Figures 5g-h** the integral for each layer at various thermal annealing times. They confirm the fast and large solvent elimination for both the upper and lower layers in the Stage-1. Moreover, XRD patterns (**Figure S11**, Supporting Information) show that, for all the samples, the initial layer is transformed into the perovskite one during this initial period.

Based on the above analysis and XRD data provided in **Figure S11** (Supporting Information), we determined that the film growth mainly occurred in Stage-2 (green zone in **Figure 5g-h**). At this stage, we observed solvent elimination at about a constant speed, and we determined the slope of the two linear fits: the SUS-2 slope for the upper layer and the SLS-2 slope for the lower layer. Then, we defined two parameters reporting the relative growth speed of each layer. The first is GI for Gap Index, defined as (SUS-2 – SLS-2)*100/Max{SUS-2,SLS-2}. SUS-2 and SLS-2 are reported in **Table 3**. By analyzing and comparing the slopes of the two curves (**Table 3**), the films' growth direction is judged and it allows to compare the differences of film growth rate between different perovskites more clearly.

Table 3. Slope parameters were extracted from the linear fit lines of the upper layer and lower layers at Stage-2.

NAME	SUS-2[a)]	SLS-2[b)]	GI[c)] [%]
Ref	-0.007	-0.002	+71.4
Au_NPs-30	-0.006	-0.007	+16.7

a) SUS-2 : The Slope of Upper layer in the Stage-2

b) SLS-2 : The Slope of Lower layer in the Stage-2

c) GI (Gap Index) = (SUS-2 – SLS-2)*100/Max{SUS-2,SLS-2}

Figures 5g-h and **Table 3** provide us the following two conclusions: 1) When the slope of the upper layer in the stage-2 (SUS-2) is very close to that of the slope of the lower layer in the stage-2 (SLS-2), it results in homogeneous films with big monolithic grains. We define this growth trend as a lateral growth. This case is encountered for the Au_NPs-30 sample (see **Figure 6b**). 2) When SUS-2 is greater than SLS-2, the film grows downward (from top to down). This kind of sample exhibit a high GI (+71.4%). The downward growth is found for Ref film (see **Figure 6a**).

Furthermore, to better understand the relationship between the growth directions and the residual solvents in the upper and lower layers, we introduced another essential parameter named MLU, defined as the Lower layer residual solvent ratio over Upper layer residual solvent ratio. They are reported at

the critical annealing times in **Table 4**. In this table, we can see that the MLU for the Ref is 3.0, which is higher than that of Au_NPs-30 (2.1). This means that after the 60s of thermal annealing time, the Lower layer RSR of the Ref sample is 3.0 times higher than the Upper layer RSR. In other words, compared to the Au_NPs-30 sample, the inner solvent of the Ref sample is not well eliminated. This underlying solvent is trapped and will be detrimental for the quality of the *meso*-TiO_2/perovskite interface.

Table 4. The relative proportion of upper layer and lower layer at late Stage-2.

NAME	Annealing time [s]	Upper layer RSR[(a)] [%]	Lower layer RSR[(b)] [%]	MLU[(c)]
Ref	60	25.0	75.0	3.0
Au_NPs-30		32.3	67.7	2.1

[(a)] Upper layer RSR (Residual Solvent Ratio) = Integral area of upper layer/(Integral area of upper layer + Integral area of lower layer)

[(b)] Lower layer RSR = Integral area of lower layer/(Integral area of upper layer + Integral area of lower layer)

[(c)] MLU (Multiple of Lower layer RSR over Upper layer RSR) = Lower layer RSR/Upper layer RSR.

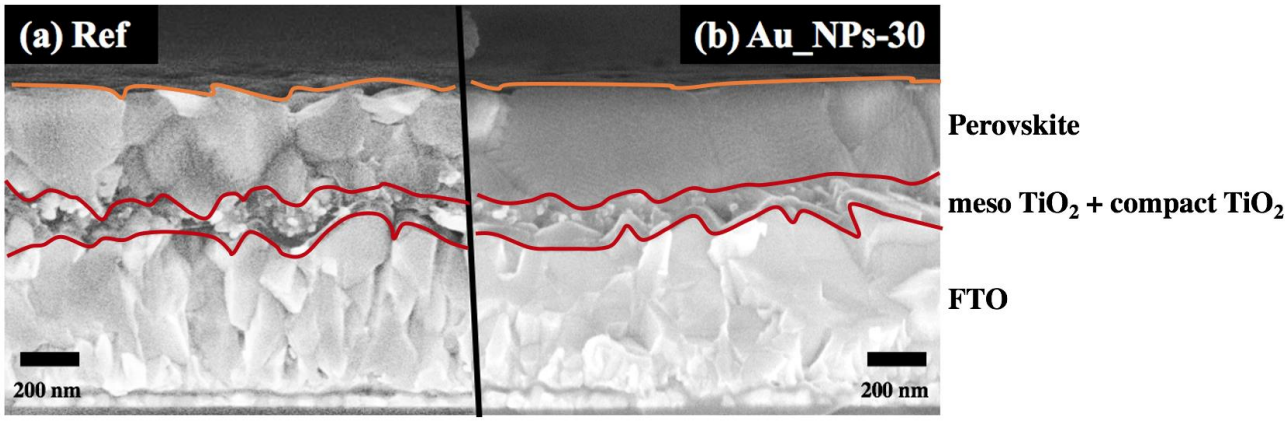

Figure 6. SEM cross-sectional views of (a) Ref and (b) Au_NPs perovskite layers deposited on glass/FTO/*c*-TiO2/*mp*-TiO_2 (the scale bar is 200 nm).

Cite this paper as : D. Zheng, C. Schwob, Z. Ouzitb, L. Coolen, Th. Pauporté, How Do Gold Nanoparticles Boost the Performance of Perovskite Solar Cells? Nano Energy, 94 (2022) 106934.
DOI: 10.1016/j.nanoen.2022.106934

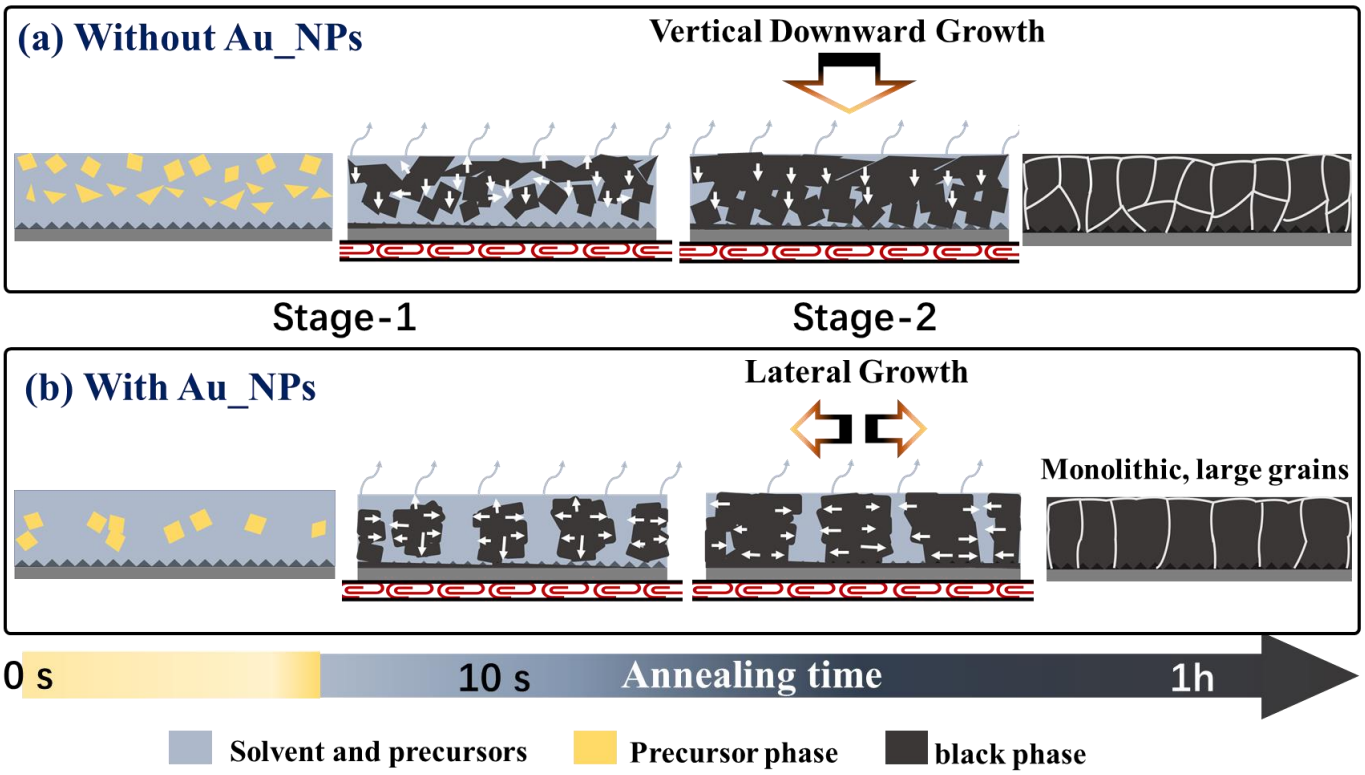

Figure 7. Schematic of the film formation processes upon thermal annealing observed for (a) Ref and (b) Au_NPs-30 samples: Grain growth direction and mechanism.

The perovskite films growth stages and mechanism, deduced from this study, are schematized in **Figure 7**. We have evidenced two stages. Upon Stage-1, perovskite nucleates, and the grains start to growth in all the directions. Upon Stage-2, a different behavior has been found depending on the presence or not of the gold nanoparticles. For the Ref sample, the solvent is better eliminated at the top and the film grows downward. It results in multiple and oblique grain boundaries and the production of relatively small perovskite grains (**Figure 7a**). For the Au_NPs-30 sample, the solvent is slowly and homogeneously eliminated in the depths of the film, which leads to the lateral growth of the grains. It results in large monolithic grains with low defect density, which is the targeted characteristics for the efficient charge transfer across the $MAPbI_3$ layer thickness (**Figure 7b**).

3. Conclusion

In this work, we successfully prepared a $MAPbI_3$ perovskite solar cell with an efficiency of 19.01% through the addition of Au_NPs. Furthermore, we improved the efficiency of the cell up to 20.44% through PAI post-treatment. Based on the above good results, we conducted a detailed analysis, combining experimental and modelling investigations, to understand the performance enhancement induced by Au_NPs additive. The optical simulation analysis indicated that, in order to enhance light absorption by LSPR effects, the Au_NP concentration would need to be 1 % volume fraction or above,

which is 100 times higher than in our optimized fabricated devices. Moreover, potential differences in $MAPbI_3$ thickness induced by the Au_NPs would only contribute weakly to the increased photovoltaic efficiency. Consequently, we attributed the increased light absorption, manifested by the *EQE* spectra, to an improvement of the intrinsic perovskite crystalline properties. The better optical, structural and crystalline qualities of the Au_NP perovskite film is evidenced by a range of AFM, SEM and XRD characterizations, while TR-PL and impedance spectroscopy have revealed the reduction of recombination due to the reduction of defects. The mechanism of film growth improvement has been then unveiled by GD-OES analysis and XRD: due to the slowdown of the solvent evaporation by the Au_NPs (as confirmed by DSC), the growth occurs laterally and more homogeneously throughout the film and yields to better crystals, large monolithic grains and less structural defects. We have then concluded that the addition of Au_NPs makes the PSC efficiency significantly enhanced, mainly because the quality of the film has been improved. If any, the enhancement due to plasmonic effects on the perovskite absorption is negligible at these concentrations.

4. Experimental Section

Preparation of Substrate, Compact TiO_2, and Mesoporous TiO_2 layers:

Fluorine-doped SnO_2 (FTO) substrates (TEC 7 from Pilkington) were etched pattern by zinc powder and 10% HCl solution before being cleaned with soap and water. The substrates were then immersed for 20 min in a concentrated 2.2M NaOH in ethanol/water (10:1 v/v %) and rinsed with deionized water in an ultrasonic bath for 15 min. The substrates were subsequently heated at 500°C for 15 min. The compact TiO_2 hole blocking layer, noted *c*-TiO_2, was prepared by aerosol spray pyrolysis [51]. The TiO_2 nanoparticle solution employed to prepare the mesoporous layer, noted *mp*-TiO_2, was prepared in advance and stirred for at least 12h.[52] The TiO_2 NR30-D paste (from Greatcell) was diluted in ethanol with a 1:7 w/w ratio. 45 µL of the solution was dropped on the *c*-TiO_2 layer and spin-coated at 2000 rpm for 15s. The layer was then dried on a hotplate at 70 °C for 5-10 min and finally heated at 500 °C under an air flux for 30 min, cooled down to 200 °C and removed from the hotplate.

Preparation of Gold Nanoparticles:

The Au NPs were obtained by a Turkevitch synthesis, based on Au(III) reduction by citrate at 100°C in water. The concentration in Au was 0.25 mM. By centrifugation of the solution, it was possible to concentrate the NPs. Then, the NPs were transferred to DMSO, the solvent employed for $MAPbI_3$ perovskite layer synthesis. 0.75 mL of DMSO was added and the solution was heated to remove the residual water. Therefore, from 189 mL of 14.3 nm sized Au NPs solution in water, we obtained 0.75

mL of a DMSO NP solution. The concentration factor was 252. This solution was dark red as expected for non-aggregated, stabilized NPs. The Au_NPs concentration was ~7.10^{-7} M, with an Au concentration of [Au]~0.06 M.

Preparation of the PVK layer:

MAPbI$_3$ layers with/without Au_NPs preparation: The MAPbI$_3$ precursor solution had a 1.35M concentration. 622.3 mg PbI$_2$, 214.6 mg MAI and 0 µL, 15 µL, 30 µL, 45 µL of Gold nanoparticles solution were mixed in 800 µL DMF and 200 µL (Ref), 185 µL (Au_NPs-15), 170 µL (Au_NPs-30), 155 µL (Au_NPs-45) DMSO, respectively.[53] The solution was stirred and kept warm at 60°C for 2h before use. The Spin-coating program was 1000 rpm for 10s and 4000 rpm for 30 s. 100 µL of chlorobenzene was dripped 30s after starting the spinning routine. The layers were finally annealed on a hotplate at 105 °C for 60 min. The best performances were achieved after the device preparation. These layers are denoted Ref, Au_NPs-15, Au_NPs-30 and Au_NPs-45.

PAI Post-treatment: The PAI post-treatment consisted of dropping 60 µL of a 4 mg/mL propylamine hydroiodide (PAI) solution onto the perovskite film after cooling. A one-step spin-coating program was employed (2000 rpm/s acceleration, 3000 rpm for the 20s). After that, the sample did not need to be reheated. The optimized treated films are noted Au_NPs-30/PAI.

Spiro-OMeTAD layer deposition: The hole transporting material (HTM) solution was prepared by dissolving 78 mg of Spiro-OMeTAD (Borun New Material Technology) in 1 mL of chlorobenzene. Then, 17.9 µL of bis(trifluoromethylsulfonyl)imide lithium salt solution (Li-TFSI) (Sigma Aldrich) solution (517 mg in 1 mL ACN), 30.4 µL of TBP (tert-butylpyridine) (Sigma Aldrich) and 14 µL of tris(2-1H-pyrazol-1-yl)-4-tert-butylpyridine)-cobalt(III) tris (bis(trifluoromethylsulfonyl)imide) (Dyesol, FK209) (376 mg in 1 mL acetonitrile) were added to this solution. 40 µL of the HTM solution was spin-coated at 4000 rpm for 30 s. Finally, the device was completed by thermally evaporating a 70-80 nm thick gold back contact on the Spiro-OMeTAD layer.

***Synthesis of adduct powders*:**

First, 0.5 mL of precursor solutions were prepared by using the recipe mentioned above. Second, 10 mL of diethyl ether was added to precipitate the corresponding adduct. The precipitates were collected and dried in N_2 filled Glovebox overnight.

Characterization methods

The XRD patterns were recorded by a PANanalytical X-Pert high-resolution X-ray diffractometer operated at 40 kV and 45 mA and using the CuKα radiation with λ= 1.5406 Å. The specular absorbance spectra were measured by a Cary 5000 UV-Vis-NIR spectrophotometer. A glass/FTO/*c*-TiO_2/*mp*-TiO_2

sample was employed for the baseline and the perovskite films were deposited on this substrate. The photoluminescence (PL) spectra were measured by a Cary Eclipse fluorescence spectrometer. The time-resolved photoluminescence (TRPL) measurements were performed under a microscope lens (numerical aperture 0.7). The perovskites layers were spin-coated onto a glass/FTO/c-TiO_2/mp-TiO_2 substrate. The top of the PVK layer was excited by a 470 nm diode laser (Picoquant) filtered by a 488-nm longpass filter. The emission was analyzed for time-resolved photoluminescence decay by a PerkinElmer SPCM avalanche photodiode combined with a Picoharp acquisition card (500 ps characteristic time of the total system response function) used with the laser in a pulsed mode at a 10 nW excitation power (pulse duration 70 ps). The morphology of the perovskite thin films was imaged using a field-emission SEM equipment (Zeiss Supra 40) in the in-lens mode. The EDX spectra were measured with a Quantax system from Brucker operated at 15 kV. Glow-Discharge Optical Emission Spectrometry (GD-OES) analyses were performed using a HORIBA Jobin Yvon GD Profiler 2 equipment.[5,54] This instrument was equipped with an RF-generator (at 13.56 MHz), a standard HORIBA Jobin Yvon glow discharge source with a cylindrical anode of 4 mm internal diameter and two optical spectrometers (a polychromator and a monochromator) for fast-optical detection. The Ar plasma was generated at an Ar pressure of 420 Pa and an applied power of 17 W. The precursor layer, the perovskite layer or the solar cell was mounted on an O-ring at one side of the plasma chamber and used as a cathode. The analyzed area was a disk 4 mm in diameter (**Figure S14**, Supporting Information).

The *J-V* curves were recorded by a Keithley 2410 digital source meter, using a 0.1 $V.s^{-1}$ voltage scan rate. The solar cells were illuminated with a solar simulator (Abet Technology Sun 2000) filtered to mimic AM 1.5G conditions (100 mW/cm^2). A black mask delimited the illuminated surface with an aperture diameter of 3 mm. The power density was calibrated at 100 $mW.cm^{-2}$ by the use of a reference silicon solar cell.[55] The tracking experiments were performed under ambient conditions. The current was followed at the voltage of the maximum power. The external quantum efficiency (*EQE*) spectra were measured using an Oriel QUANTX-300 system. The light beam was chopped at 77Hz. A NIST-calibrated Si photodiode calibrated the monochromatic illumination. The sample morphologies were examined with a high-resolution Ultra 55 Zeiss FEG field-emission scanning electron microscope (FE-SEM) in the in-lens mode. The electrical impedance spectra were measured at room temperature, between 1 MHz and 100 mHz, with a 20 mV AC signal, using a PGSTAT 12 apparatus from Autolab. All the measured cells had the same contact geometries. The impedance spectra were measured at room temperature, over a large applied voltage (Vappl) range, under a ~0.9 sunlight power density supplied by a halogen Schott lamp. A 0.16 cm^2 mask delimited the cell illuminated area. The spectra were analyzed using the Z-view software from National Instrument.

Simulation methods

The Mie absorption coefficients (**Figure 2b**) were calculated using a free code published in Ref.[56]. The numerical FDTD simulations (**Figure 2c**) were performed with the commercial software Lumerical, using a mesh size of 2 nm, with electromagnetic planar wave excited in the bottom plane, transmission probed in the upper plane, and phase-matching layers on the sides. The transfer-matrix simulations (**Figure S6,** Supporting Information) were performed with the commercial software Film Wizard. We used a water refractive index of 1.33, the gold index tabulated in Ref.[57], and the $MAPbI_3$ optical index reported in Ref.[58]. The full solar cell was described by a layered optical model established in Ref.[49].

Acknowledgements

Dr Philippe Vermaut (IRCP, Chimie-Paristech, France) is acknowledged for access to the DSC 3 apparatus from STAR System. The PhD scholarship of Mr D. Zheng was funded by the CSC-Paristech program (grant number 201806310126). The ANR agency is acknowledged for financial support via the Moreless project ANR-18-CE05-0026 and the ChemSta project ANR-21-CE05-0022.

References

[1] M.L. Michael, T. Joel, N.M. Tskurou, J.S. Henry, Science 338 (2012) 643-647.

[2] K. Hui-Seon, L. Chang-Ryul, I. Jeong-Hyeok, L. Ki-Beom, M. Thomas, M. Arianna, M. Soo-Jin, H. Robin, Y. Jun-Ho, E. Jacques, G. Michael, P. Nam-Gyu, Sci. Rep. 2 (2012) 591.

[3] B. Julian, P. Norman, M. Soo-Jin, H. Robin, G. Peng, Nature 499 (2013) 316.

[4] Z. Huangping, C. Qi, L. Gang, L. Song, S. Tze-bing, D. Hsin-sheng, H. Ziruo, Y. Jingbi, L. Yongsheng, Y. Yang, Science 345 (2014) 542-546.

[5] D. Zheng, T. Pauporté J. Mater Chem. A 9 (2021) 17801-17811.

[6] J. Zhang, J. Emilio, I. Mora-Sero, B. Viana, T. Pauporté, J. Mater. Chem. A 3 (2015) 4909–4915.

[7] D. Zheng, Z. Tao, Th. Pauporté, Solar RRL (2021) 2100010.

[8] D. Zheng, T. Zhu, Th. Pauporté, ACS Appl. Energy Mater. 3 (2020) 10349−10361.

[9] Z. Fei, Z. Kai, Adv. Energy Mater. 10 (2020) 1902579.

[10] A. Leblanc, N. Mercier, M. Allain, J. Dittmer, V. Fernandez, Th. Pauporté, Angew. Chem. Int. Ed. 56 (2017) 16067–16072.

[11] D. Pitarch-Tena, N. Thi-Tiyen, V. Marta, Th. Pauporté, ACS Energy Lett. 3 (2018) 1044−1048.

[12] NREL Chart (October 2021) https://www.nrel.gov/pv/cell-efficiency.html

[13] H. A. Atwater, A. Polman, Nat. Mater. 9 (2010) 205−213.

[14] J. A. Schuller, E. S. Barnard, W. Cai, Y. C. Jun, J. S. White, M. L. Brongersma, Nat. Mater. 9 (2010) 193−204.

[15] T. Kume, S. Hayashi, H. Ohkuma, K. Yamamoto, Jpn. J. Appl. Phys. 34 (1995) 6448−6451.

[16] O. Stenzel, A. Stendal, K. Voigtsberger, C. von Borczyskowski, Sol. Energy Mater. Sol. Cells 37 (1995) 337−348.

[17] V. E. Ferry, J. N. Munday, H. A. Atwater, Adv. Mater. 22 (2010) 4794−4808.

[18] R. A. Pala, J. White, E. Barnard, J. Liu, M. L. Brongersma, Adv. Mater. 21 (2009) 3504−3509.

[19] D.J. Aberasturi, A.B. Serrano-Montes, L.M. Liz-Marzań, Adv. Opt. Mater. 3 (2015) 602−617.

[20] K. R. Catchpole, A. Polman, Appl. Phys. Lett. 93 (2008) 191113.

[21] I. M. Pryce, D. D. Koleske, A. J. Fischer, H. A. Atwater, Appl. Phys. Lett. 96 (2010) 153501.

[22] J.-L. Wu, F.-C. Chen, Y.-S. Hsiao, F.-C. Chien, P. Chen, C.-H. Kuo, M. H. Huang, C.-S. Hsu, ACS Nano 5 (2011) 959−967.

[23] X. Yang, C.-C. Chueh, C.-Z. Li, H.-L. Yip, P. Yin, H. Chen, W.-C. Chen, A. K.-Y. Jen, Adv. Energy Mater. 3 (2013) 666−673.

[24] Q. Gan, F. J. Bartoli, Z.H. Kafafi, Adv. Mater. 25 (2013) 2385−2396.

[25] S. D. Standridge, G. C. Schatz, J. T. Hupp, J. Am. Chem. Soc. 131 (2009) 8407−8409.

[26] S. Y. Sun, T. Salim, N. Mathews, M. Duchamp, C. Boothroyd, G. C. Xing, T. C. Sum, Y. M. Lam, Energy Environ. Sci. 7 (2014) 399.

[27] W.S. Yang, J.H. Noh, N.J. Jeon, Y.C. Kim, J. Ryu, S. Seo, S.I. Seok, Science 348 (2015) 1234.

[28] P. Li, X. Jiang, S. Huang, Y. Liu, N. Fu, Surf. Interfaces 25 (2021) 101287.

[29] Y. H. Jang, Y. J. Jang, S. Kim, L. N. Quang, K. Chung, D. H. Kim, Chem. Rev. 116 (2016) 14982.

[30] Y.-F. Li, Z.-L. Kou, J. Feng, H.-B. Sung, Nanophotonics 9 (2020) 3111.

[31] K. Chan, M. Wright, N. Elumalai, A. Uddin, S. Pillai, Adv. Optical Mater. 5 (2017) 1600698.

[32] M. A. Alkhalayfeh, A. A. Aziz, M. Z. Pakhuruddin, K. M. Katubi, M. Spiky, Phys. Status Solidi A 218 (2021) 2100310.

[33] J.-D. Chen, T.-Y. Jin, Y.-Q. Li, J.-X. Tang, Nanoscale 11 (2019) 18517.

[34] G. Kakavelakis, K. Petridis, E. Kymakis, J. Mater. Chem. A 5 (2017) 21604.

[35] R. S. Moakhar, S. Gholipour, S. Masudy-Panah, A. Seza, A. Mehdikhani, N. Riahi-Noori, S. Tafazoli, N. Timasi, Y.-F. Lim, M. Saliba, Adv. Sci. 7 (2020) 1902448,

[36] W. Zhang, M. Saliba, S. D. Stranks, Y. Sun, X. Shi, U. Wiesner, H. J. Snaith, Nano Lett. 13 (2013) 4505.

[37] M. Chun, L. Changxu, J. Huang, Y. Ma, Z. Liu, L. Li, D. Thomas, H. Yu, F. Andrea, W. Tom, Sol. RRL (2019) 1900138.

[38] G. Grancini, Roldán-Carmona; C. I. Zimmermann, E. Mosconi, X. Lee, D. Martineau, S. Narbey, F. Oswald, F. De Angelis, M. Graetzel, M. K. Nazeeruddin, Nature Commun. 8 (2017) 15684.

[39] T. Li, Y. Pan, Z. Wang, Y. Xia, Y. Chen, W. Huang, J. Mater. Chem. A 5 (2017) 12602.

[40] Q. Pingli, W. Tong, W. Zhengchun, Lanxiao. L, M. Liang, Feihong. X. Lun, C. Xiangbai, L. Haixia, Y. Xueli, F. Guojia. Adv. Funct. Mater. 30 (2020) 1908408.

[41] A. Bayles, S. Carretero-Palacios, L. Calio, G. Lozano, M.E. Calvo, H. Miguez, J. Mater. Chem. C 8 (2020) 916-921.

[42] K. Yao, H. Zhong, Z. Liu, M. Xiong, S. Leng, J. Zhang, Y. Xu, W. Wang, L. Zhou, H. Huang, A. Jen, ACS Nano 13 (2019) 5397−5409.

[43] M. Xiaoqian, M. Ben, Y. Tianyan, X. Xin, Z. Liuquan, W. Wie, C. Kun, D. Lingling, C. Shufen, H. Wei, ACS Appl. Energy Mater. 2 (2019) 3605−3613.

[44] W. Runsheng, Y. Bingchu, Z. Chujun, H. Yulan, C. Yanxia, L. Peng, Z. Conghua, H. Yuying, Y. Junliang, J. Phys. Chem. C 120 (2016) 6996−7004.

[45] C. Wunjhen, L. Yuchang, K. Gautham, X. Shunyu, C. Fangchung, Synthetic Metals 273 (2021) 116675.

[46] H. Zhiyuan, Z. Chi, M. Rangwei, L. Xuanhui, C. Mengwei, L. Haifei, Y. Yingping, Nanomaterials 10 (2020) 2364

[47] D. Zheng, T. Pauporté, J. Mater Chem. A 9 (2021) 17801-17811.

[48] S. Li, Z. Liu, Z. Qiao, X. Wang, L. Cheng, Y. Zhai, Q. Xu, Z. Li, K. Meng, G. Chen, Adv. Funct. Mater. 30 (2020) 2005846.

[49] C. Ma, D. Zheng, D. Demaille, B. Gallas, C. Schwob, Th. Pauporté, L. Coolen, Sol. Energy Mater. Sol. Cells 230 (2021) 111144.

[50] Y. Guo, K. Shoyama, W. Sato, Y. Matsuo, K. Inoue, K. Harano, C. Liu, H. Tanaka, E. Nakamura, J. Am. Chem. Soc. 137 (2015) 15907-15914.

[51] P. Wang. Z. Shap, M. Ulfa, Th. Pauporté, J. Phys. Chem. C 121 (2017) 9131–9141.

[52] T. Pauporté, A. Goux, A. Kahn-Harari, N. de Tacconi, K. Rajeshwar, D. Lincot, J. Phys. Chem. Solids, 64 (2003) 1737-1742.

[53] F. Cheng, J. Zhu, Th. Pauporté, ChemSusChem 14 (2021) 3665–3692.

[54] H. Lee, S. Gaiaschi, P. Chapon, A. Marronnier, H. Lee, J.C. Vanel, D. Tondelier, J.E. Bouree, Y. Bonnassieux, B. Geffroy, ACS Energy Lett. 2 (2017) 943-949.

[55] Y. Kusumawati, M. A. Martoprawiro, Th. Pauporté, J. Phys. Chem. C 118 (2014) 9974–9981.

[56] C.F. Bohren, D.R. Huffman, J. Wiley (1983).

[57] P.B. Johnson, R.W. Christy, Phys. Rev. Letters 11 (1963) 541.

[58] S. Manzoor, J. Hausele, K.A. Bush, A.F. Palmstrom, J. Carpenter, Z.J Yu, S.F. Bent, M.D. Mcgehee, Z.C. Holman, Opt. Express 21 (2018) 27441-27460.

Authors information

Daming ZHENG received his Ph.D. degree from Chimie ParisTech, PSL Research University, in 2021. Now, he is post-doctor at both PSL Research University and Sorbonne Université. His main research activities focus on using perovskite growth additives and adjusting chemical composition, as well as interfacial engineerings for high-performance and stable solar cells.

Cite this paper as : D. Zheng, C. Schwob, Z. Ouzitb, L. Coolen, Th. Pauporté, How Do Gold Nanoparticles Boost the Performance of Perovskite Solar Cells? Nano Energy, 94 (2022) 106934. DOI: 10.1016/j.nanoen.2022.106934

Catherine SCHWOB is a professor at Sorbonne Universite and works at the Institut des NanoSciences de Paris (Sorbonne Universite, CNRS). She received a PhD in quantum optics (Laboratory Kastelr Brossel, University Pierre et Marie Curie) in 1997. Her research activities focused on plasmonics and nanophotonics including sensing, plasmonic resonators, detection of chiral molecules.

Yoann PRADO (born in 1980, Paris, France) received his PhD in 2010 under the supervision of Dr L. Catala and Prof. T. Mallah (ICMMO, Université Paris-Sud). He worked as a postdoctoral fellow at ICMol with Prof. E. Coronado (Universitat de Valencia, 2011-2013), then at Sorbonne Université with Dr Jérôme Fresnais (Phenix, 2013-2014 & 2016-2018), and in Centre de Recherche Paul Pascal with Dr R. Clérac (Université de Bordeaux, 2014-2015). Since 2018, he is a CNRS engineer at the Institut des NanoSciences de Paris - Sorbonne Université, working on metallic and semiconductors nanoparticles synthesis.

Zakarya OUZIT is a current PhD student under the supervision of Dr Laurent Coolen at Institute of NanoSciences of Paris (INSP), Sorbonne Université. He graduated both from Ecole Normale Supérieure de Lyon and Sorbonne Université in optics and light-matter interactions (2020). His research interests include the collective behavior of semiconducting nanoparticles and investigating the effect of self-assemblies on their optical properties.

Laurent COOLEN is an associate professor at Sorbonne University and he works at the Institut de NanoSciences de Paris. He received his Ph.D. in Solid States Physics from Université Denis Diderot, Paris, France in 2006. His research interests include the fluorescence properties of nanoparticles and the influence of their photonic or plasmonic environment.

Cite this paper as : D. Zheng, C. Schwob, Z. Ouzitb, L. Coolen, Th. Pauporté, How Do Gold Nanoparticles Boost the Performance of Perovskite Solar Cells? Nano Energy, 94 (2022) 106934. DOI: 10.1016/j.nanoen.2022.106934

Thierry PAUPORTÉ is a director of research at the Centre National de la Recherche Scientifique (CNRS) in France and he works at Chimie-Paristech, PSL Université. He is graduated in Chemistry from the École Normale Supérieure de Lyon (ENS-L). He received his Ph.D in physical chemistry from Montpellier II University, France, in 1995. His research interests include oxide and perovskite semiconductors, the functionalizing of the materials surfaces and he works on the integration of films and structures in efficient devices. The applications studied include light emitting diodes, perovskite solar cells, dye-sensitized solar cells, nanosensors, photodetectors, photocatalysis, wettability and fouling.

Cite this paper as : D. Zheng, C. Schwob, Z. Ouzitb, L. Coolen, Th. Pauporté, How Do Gold Nanoparticles Boost the Performance of Perovskite Solar Cells? Nano Energy, 94 (2022) 106934.
DOI: 10.1016/j.nanoen.2022.106934
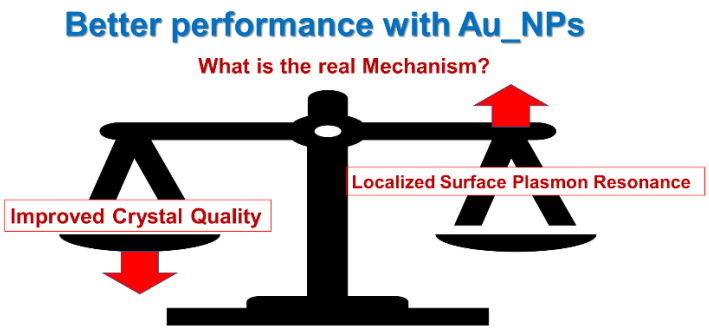
Graphical abstract